# High fracture toughness micro-architectured materials

Y. Liu[a], L. St-Pierre[b,c], N.A. Fleck[b], V.S. Deshpande[b,*], A. Srivastava[a,**]

[a]*Department of Materials Science and Engineering, Texas A&M University, College Station, TX, USA*
[b]*Department of Engineering, University of Cambridge, Cambridge CB2 1PZ, UK*
[c]*Department of Mechanical Engineering, Aalto University, Espoo, FI*

**Abstract**

We investigate the possibility of achieving high fracture toughness and high strength by the design of lightweight (density below water) metallic micro-architectured materials. The micro-architectured materials were manufactured by drilling a hexagonal array of holes in plates of an aluminum alloy, and the fracture toughness was evaluated via three-point bend tests of single-edge notch specimens. The results show that the fracture toughness of micro-architectured materials increases with increasing relative density and remarkably, a micro-architectured material can be 50% lighter than the parent material but maintain the same fracture toughness. Additional tests on geometrically similar specimens revealed that the fracture toughness increases linearly with the square-root of the cell size. The experiments are complemented by finite element calculations of ductile fracture. In the calculations, the fracture toughness of single-edge notch specimens subjected to three-point bending are evaluated using both, a procedure similar to the experiments and direct computation of the $J$-contour integral. The fracture toughness as calculated by both methods are consistent with the experimental results. In addition, the calculations are also carried out for single-edge notch specimens subjected to tensile loading, confirming the validity of the measured fracture toughness as a useful material property independent of specimen geometry.

*Keywords:* Crack propagation and arrest; Fracture toughness; Mechanical testing; Micro-architectured materials; Finite elements

## 1. Introduction

The demand for lower fuel consumption and $CO_2$ emission while increasing the safety and reliability in the transportation and aerospace industries have driven the development of new lightweight materials with high strength and fracture toughness. Accordingly, the number of materials has increased dramatically: there are now over 120,000 different materials (Ashby, 2005). But is there still room for further improvement? To answer this question, it is insightful to consider material property charts (Ashby, 2005), with axes in the form of

*Email address: vsd20@cam.ac.uk (V.S. Deshpande)
**Email address: ankit.sri@tamu.edu (A. Srivastava)

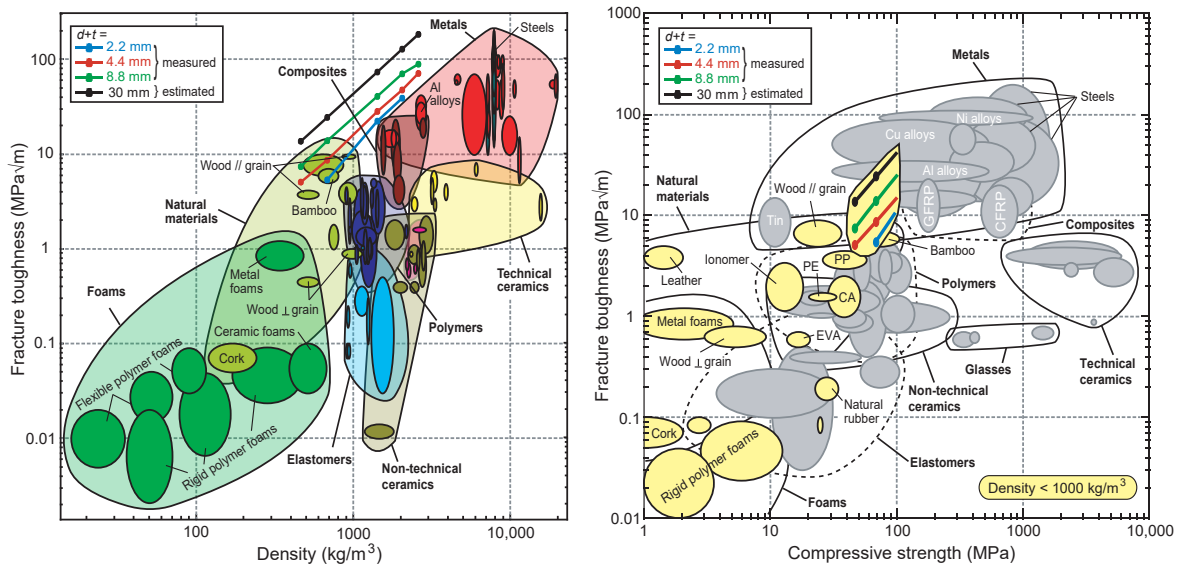


(a) (b)

Figure 1: Material property charts of (a) fracture toughness versus density and (b) fracture toughness versus compressive strength. The properties of micro-architectured materials consisting of hexagonal array of holes with hole spacing $d + t$, manufactured and tested in this work and the estimated properties of a micro-architectured material with $d + t = 30$mm are also shown for comparison. The abbreviations are CA: cellulose polymer; EVA: ethylene vinyl acetate; PE: polyethylene; PP: polypropylene; CFRP: carbon fiber reinforced polymer; GFRP: glass fiber reinforced polymer. In (b) materials with density less than 1000kg/m$^3$ are shaded in yellow.

material properties. For example, a chart of fracture toughness versus density is shown in Fig. 1(a), and one of fracture toughness versus compressive strength is shown in Fig. 1(b). Metals are clearly the toughest materials, but they are also the heaviest, Fig. 1(a). The choice of lightweight materials is limited: only foams, natural materials and a few elastomers and polymers have density less than water (1000kg/m$^3$). The scarcity of lightweight materials is emphasized in Fig. 1(b), where solids with density less than 1000kg/m$^3$ are highlighted. Among these lightweight materials, wood and bamboo offer the best combination of fracture toughness and strength. This raises an important question: how can the current material space be extended? Here, we explore the possibility of achieving lightweight, high fracture toughness and high strength by the design of micro-architectured materials.

The potential of micro-architectured and lattice materials to combine high stiffness and strength at low densities is well documented, see for example, Fleck et al. (2010); Ashby (2011); Khaderi et al. (2014); Dong et al. (2015); Gu and Greer (2015); Khaderi et al. (2017). However, less is known about their capacity for high fracture toughness at low density. Experimental, analytical and numerical studies (Maiti et al., 1984; Huang and Gibson, 1991b,a; Gibson and Ashby, 1999; Fleck and Qiu, 2007; Romijn and Fleck, 2007; Quintana-Alonso et al., 2010) have shown that the mode I fracture toughness, $K_{IC}$, of two-dimensional micro-architectured materials made from an elastic-brittle material of fracture

strength, $\sigma_f$, can be expressed as:

$$K_{IC} = H\sigma_f \bar{\rho}^h \sqrt{l} \tag{1}$$

where $\bar{\rho}$ and $l$ are the relative density and cell size of the micro-architectured material, respectively, and $H$ and $h$ are constants dependent upon the topology of the micro-architectured material. Numerical results of Schmidt and Fleck (2001) and experimental results of O'Masta et al. (2017) suggest that Eq. (1) can also be applied to ductile micro-architectured materials made from an elastic-plastic material. However, these studies only considered micro-architectured materials of low relative density, $\bar{\rho} \lessapprox 0.2$. Here, we present fracture toughness tests on ductile micro-architectured materials with a wide range of relative densities, $0.17 \leq \bar{\rho} \leq 0.95$. We find that micro-architectured materials can achieve a higher fracture toughness than that of the parent solid. Thus, micro-architectured materials can have a combination of properties that outperform other engineering and natural materials, Fig. 1.

A schematic of the micro-architectured material considered in this work that comprise a hexagonal array of holes drilled in the plates of an aluminum alloy is shown in Fig. 2. The relative density of the micro-architectured material is given by:

$$\bar{\rho} = 1 - \frac{\sqrt{3}\pi d^2}{6(d+t)^2} \tag{2}$$

where $d$ is the hole diameter and $d + t$ is the hole spacing. First, we varied the hole diameter while keeping the hole spacing fixed at $d + t = 4.4$mm. We tested five specimens with $d = 4.2,\ 4.0,\ 3.2,\ 2.3$ and $1.0$mm corresponding to $\bar{\rho} = 0.17,\ 0.25,\ 0.52,\ 0.75$ and $0.95$, respectively. Second, we investigated the effect of the hole spacing on the fracture toughness by testing micro-architectured materials that are geometrically similar but half in size ($d + t = 2.2$mm) or double in size ($d + t = 8.8$mm).

For the micro-architectured material in Fig. 2, it can be hypothesized that the fracture toughness is governed by the two competing mechanisms: crack blunting and hole-hole interaction. *Crack blunting*: the holes will blunt the crack-tip and consequently, we can expect the fracture toughness to increase with increasing hole diameter (Rice, 1968; Begley et al., 1977; Yoda, 1987). *Hole-hole interaction*: consider the case of multiple holes with a fixed spacing $d + t$. Increasing the hole diameter $d$ reduces the wall thickness $t$ and as a result, we can expect the fracture toughness to decrease with increasing hole diameter. To investigate these two mechanisms independently, tests on two simpler geometries were also conducted. First, the toughening effect of crack blunting was quantified by testing specimens with a single hole at the crack-tip (Fig. 2 bottom left). Then, the second mechanism, hole-hole interaction, was introduced by testing specimens with a single row of holes (Fig. 2 bottom right). Specimens with a single hole and those with a row of holes had the same overall dimensions as the specimens of the micro-architectured material to allow comparison between the three types of specimens. All tests were done on single-edge notch specimens loaded under three-point bending as shown in Fig. 2. The geometry and dimensions of the

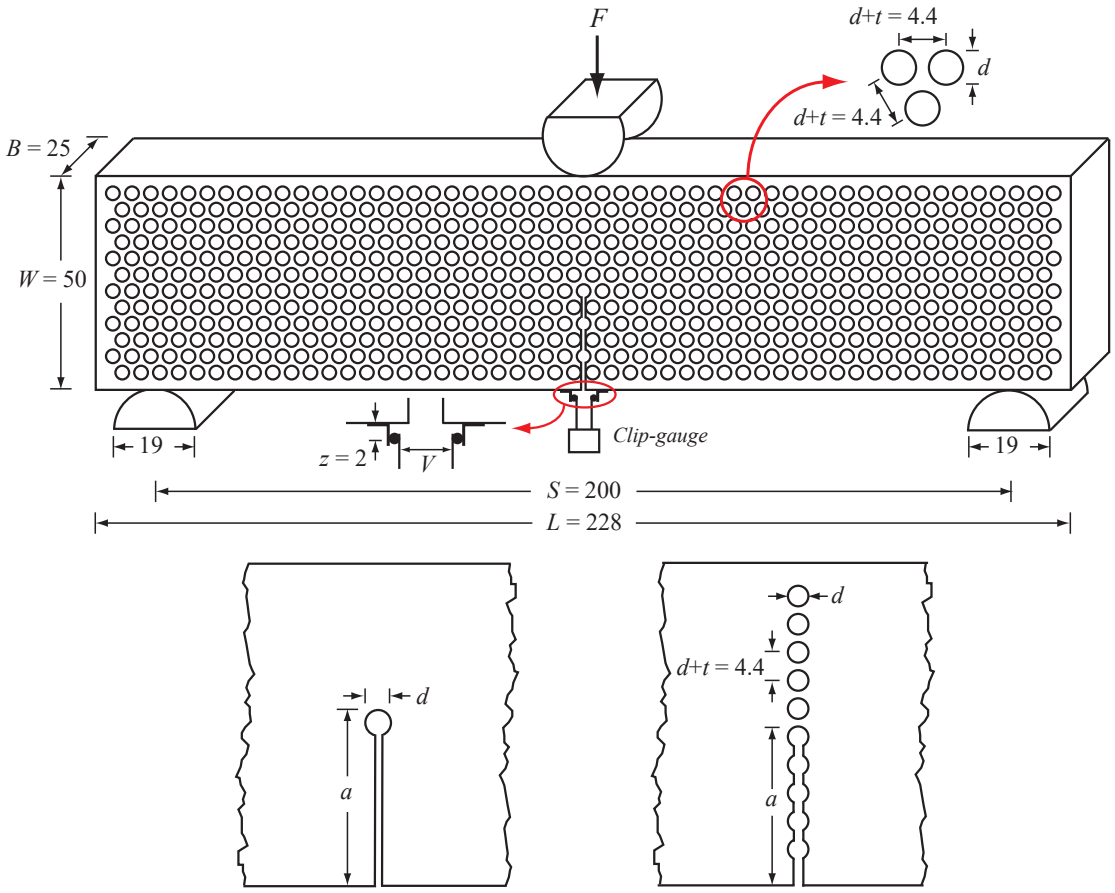


Figure 2: Schematic showing a single-edge notch specimen of a micro-architectured material consisting of a hexagonal array of holes drilled in a plate of an aluminum alloy and subjected to the three-point bending fracture test. Two simpler geometries, a single hole (bottom left) and a row of holes (bottom right) ahead of the initial crack were also tested to get more insight into the crack growth mechanisms in the micro-architectured material. For simplicity, only the central portion of the simpler geometries are shown but they had the same dimensions as the micro-architectured material. All dimensions in the figure are in mm.

specimen, and the test procedure utilized are in compliance with the ASTM standard test method for measurement of fracture toughness (ASTM:E1820-11, 2011).

Although the fracture tests of micro-architectured materials are carried out in compliance with the ASTM standard (ASTM:E1820-11, 2011). Is a standard test procedure that was initially established for specimens of bulk materials also applicable to micro-architectured materials? To gain additional insight, we have also carried out finite element calculations of ductile fracture in the specimens of the micro-architectured materials and in specimens with a single and a row of holes using a constitutive framework for progressively cavitating ductile solids. In the finite element calculations, the fracture toughness of single-edge notch specimens subjected to three-point bending are evaluated using a procedure that mimics the ASTM standard (ASTM:E1820-11, 2011) and also via direct computation of the $J$-

integral. The fracture toughness computed from the finite element calculations using both the procedures are found to be consistent with the experimental results. In addition, the finite element calculations of ductile fracture in micro-architectured materials are also carried out for single-edge notch specimens subjected to tensile loading; the same scaling between fracture toughness and relative density of the micro-architectured materials is predicted for the tensile tests and three-point bending tests. Consequently, the fracture toughness of the micro-architectured materials measured here can be treated as a material property.

## 2. Experimental method

All specimens were made from aluminum alloy 6082-T6. The single-edge notch specimens were of length, $L = 228$mm, width, $W = 50$mm and thickness, $B = 25$mm (see Fig. 2), in compliance with ASTM:E1820-11 (2011). The three types of specimens were manufactured following the same procedure. First, rectangular blocks of dimensions $L \times W \times B$ were machined from a plate. Second, the holes were drilled using a Computer-Numerically-Controlled (CNC) machine. Third, the initial crack was cut using Electrical Discharge Machining (EDM) with a wire diameter of 0.3mm.

The specimens were tested in three-point bending with a span $S = 4W = 200$mm, Fig. 2. Steel rollers of diameter of 19mm were used to provide simple support and for load introduction at mid-span. The tests were done with a screw-driven test machine at a constant cross-head displacement rate of 0.1mm/min. The force, $F$, applied at mid-span was measured by the load-cell of the test machine and the crack mouth opening displacement (CMOD) was measured by a clip-gauge. The clip-gauge was held in place by anvils of height $z = 2$mm as shown schematically in Fig. 2. Consequently, the extension measured by the clip-gauge, $V$, is related to CMOD using the relation (Anderson, 2017):

$$\text{CMOD} = \frac{r_p(W-a)+a}{r_p(W-a)+a+z}V \tag{3}$$

where the plastic rotational factor $r_p = 0.44$, the width of the specimen $W = 50$mm and the crack length is $a$.

The $J-R$ curve was evaluated using the elastic compliance method (ASTM:E1820-11, 2011). This procedure was applied directly for tests done on specimens with a single hole. However, for specimens with a row of holes and hole diameter exceeding 1mm the relation between the elastic compliance and the crack length was inaccurate and alternatively empirical relations were derived as follows. First, the crack length, $a$, was measured with a vernier. Second, the crack mouth elastic compliance, $C$, was measured using the same experimental setup as that used for the fracture toughness test, Fig. 2. Next, ten measurements of the elastic compliance were taken and the mean was calculated. Finally, the ligament ahead of the crack tip was cut with a hacksaw to extend the crack length by $\Delta a = d + t = 4.4$mm and the procedure was repeated for this new value of crack length to obtain a relation between normalized crack length, $a/W$, and normalized elastic compliance, $\bar{C} = \left(2\sqrt{BWEC/S}+1\right)^{-1}$, where $E$ is the Young's modulus. Note that the normalized

elastic compliance, $\bar{C}$, is the same non-dimensional group as employed in ASTM:E1820-11 (2011). For specimens of micro-architectured material, there was a load-drop following the fracture of a cell wall and the current crack length was directly inferred (and confirmed by visual inspection).

The stress intensity factor is related to the $J$-integral by (Rice, 1968):

$$K_J = \sqrt{E' J} \tag{4}$$

where $E' \equiv E/(1-\upsilon^2)$ is the plane strain elastic modulus. For single hole specimens and those with a row of holes, the Young's modulus, $E = 70$GPa, and the Poisson's ratio, $\upsilon = 0.33$, are the material properties of aluminum alloy 6082-T6. In contrast, for micro-architectured materials, $E'$ was taken as the effective plane strain Young's modulus of the micro-architectured material and was evaluated from the elastic unloading compliance of the single-edge notch bend specimens. Furthermore, to visualize the path and shape of the crack, partially fractured specimens of micro-architectured materials were also analyzed using scanning electron microscope (SEM) and X-ray tomography.

For comparison purposes, the deformation and fracture response of the as-received plates of the solid aluminum alloy 6082-T6 were also characterized using uniaxial tensile tests and standard fracture tests as per ASTM:E1820-11 (2011). The 0.2% offset tensile yield strength, $\sigma_Y$, of the material was found to be $\approx$ 280MPa. Following yield, the material exhibits a moderate degree of strain hardening up to an ultimate tensile strength of $\approx$ 360MPa at a strain of about 11%. The $J-R$ curve of the aluminum alloy 6082-T6 was measured by testing fully-dense specimens with a fatigue pre-crack and overall dimensions ($L$, $W$ and $B$) as indicated in Fig. 2. The fracture toughness of the as-received material was thereby measured to be, $K^S_{J_{IC}} = 27\text{MPa}\sqrt{m}$.

## 3. Experimental results

The three-point bending response of specimens with a single hole is shown in Fig. 3(a), where the force, $F$, applied at mid-span is plotted as a function of CMOD. The results are given for the hole diameter, $d = 2.3$ and 4.0mm. Both specimens display an elastic-plastic response up to a peak load $F_{pk}$ at a crack mouth opening displacement $\text{CMOD}_{pk}$. The peak load is mildly sensitive to the hole diameter, whereas $\text{CMOD}_{pk}$ increases significantly with increasing hole diameter. At peak load, a sharp crack initiates from the hole and causes an abrupt load-drop. Subsequently, quasi-static crack growth leads to a softening response in the load versus CMOD curve. The crack growth resistance curves for the two specimens are also shown in Fig. 3(a): the stress intensity factor, $K_J$, normalized by the fracture toughness of the parent material, $K^S_{J_{IC}}$, is plotted as a function of crack extension, $\Delta a$. Note that the required stress intensity for the onset of crack growth for both cases exceeds that of the parent material ($K_{J_{IC}}/K^S_{J_{IC}} > 1$). In addition, the $K^S_{J_{IC}}$ increases with increasing hole diameter, $d$. This toughening effect is due to crack tip blunting.

We now present the effect of the interaction of multiple holes on fracture toughness in Fig. 3(b), where the three-point bending response of specimens with a row of holes is shown

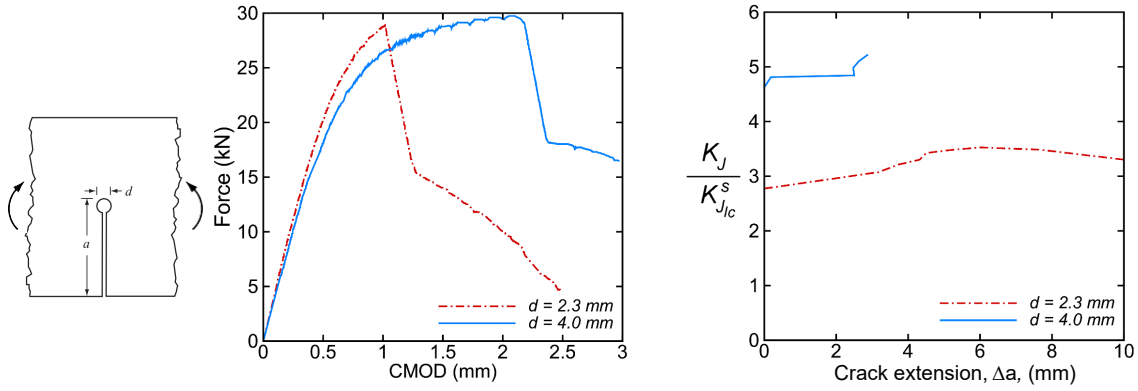


(a)

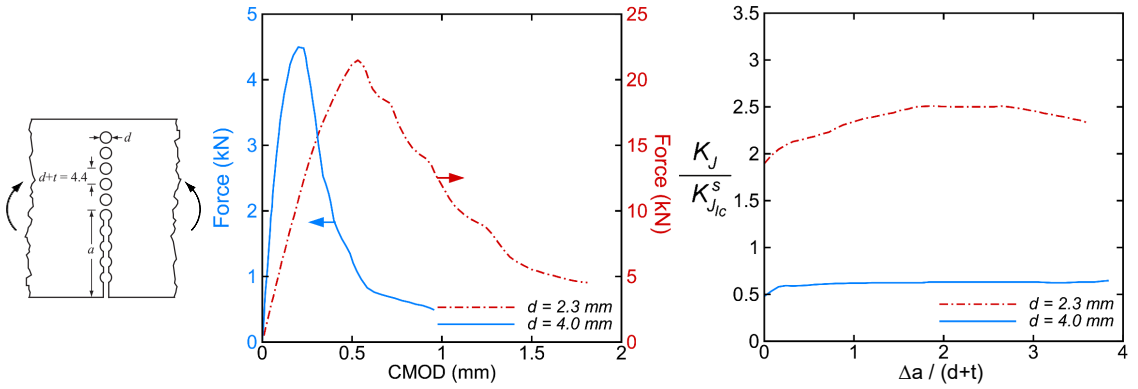


(b)

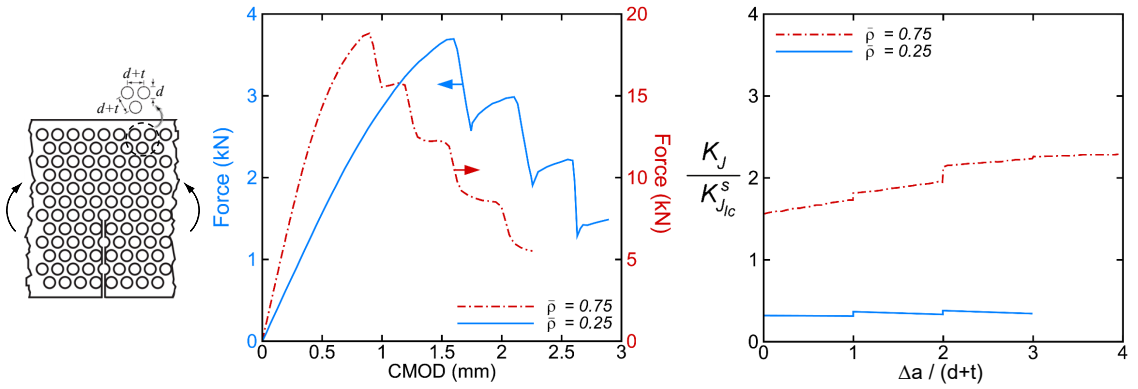


(c)

Figure 3: Results of fracture toughness tests on (a) specimens with a single hole, (b) specimens with a row of holes and (c) specimens of micro-architectured materials. For each type of specimen, a sketch of the geometry (left), the three-point bending, force - crack mouth opening displacement (CMOD) response (middle), and the crack growth resistance curves (right) are shown. The hole diameter, $d = 2.3$mm, for micro-architectured material with relative density, $\bar{\rho} = 0.75$, and $d = 4.0$mm for $\bar{\rho} = 0.25$. The hole spacing, $d + t = 4.4$mm, for the specimens with a row of holes and the micro-architectured materials.

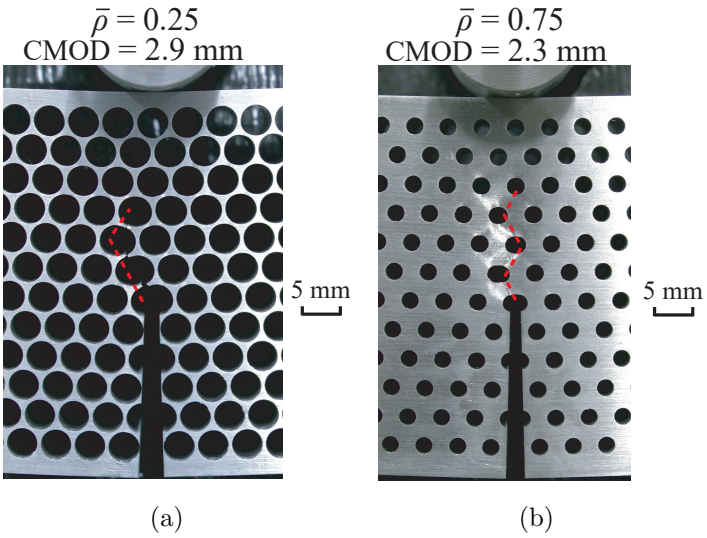


Figure 4: Surface images of deformed specimens of micro-architectured materials: (a) with a relative density, $\bar{\rho} = 0.25$, and deformed under three-point bending to a crack mouth opening displacement (CMOD) of 2.9mm; and (b) with $\bar{\rho} = 0.75$ and deformed to CMOD= 2.3mm. In both (a) and (b), the crack path is shown by a dashed red line. The hole diameter, $d = 2.3$mm, for micro-architectured material with $\bar{\rho} = 0.75$ and $d = 4.0$mm for $\bar{\rho} = 0.25$. The hole spacing, $d + t = 4.4$mm, for both the specimens.

for two selected values of hole diameter, $d = 2.3$ and 4.0mm. Both specimens have an elastic-plastic response up to a peak load $F_{pk}$ at which point crack growth initiates. Subsequently, there is a softening response as the crack extends. The normalized crack growth resistance curves for both specimens with a row of holes are also shown in Fig. 3(b). Here, the crack extension $\Delta a$ has been normalized by the hole spacing, $d + t = 4.4$mm. A comparison of Figs. 3(b) and 3(a) shows that the fracture toughness of specimens with a row of holes is less than that of the specimens with a single hole. Also, in contrast to the single hole specimens, the toughness of specimens with a row of holes decreases with increasing hole diameter, $d$. This is due to the fact that the wall thickness, $t$, decreases with increasing $d$ since the hole spacing is kept fixed at $d + t = 4.4$mm. Despite this knockdown in fracture toughness, a promising result emerges from Fig. 3(b): the specimen with $d = 2.3$mm requires a critical stress intensity for crack growth exceeding that of the parent material ($K_{J_{IC}}/K^S_{J_{IC}} > 1$).

Next, we investigate whether micro-architectured materials can exhibit a fracture toughness that exceeds the parent material. The three-point bending responses of single-edge notch specimens of micro-architectured materials with relative densities, $\bar{\rho} = 0.25$ and 0.75 are shown in Fig. 3(c). Both specimens exhibit an elastic-plastic response up to a peak load $F_{pk}$ at which point the cell wall at the crack-tip fails and a sharp load-drop ensues. Additional plastic deformation occurs under increasing load for $\bar{\rho} = 0.25$, and at roughly constant load for $\bar{\rho} = 0.75$, until the next cell wall fractures. The normalized crack growth resistance curves for both micro-architectured materials are included in Fig. 3(c). Both curves have a step-like shape because the crack extends suddenly by $\Delta a = d + t = 4.4$mm when a cell

wall fails. The shape of the resistance curve is sensitive to relative density: the resistance curve is almost flat for $\bar{\rho} = 0.25$, whereas it rises considerably for $\bar{\rho} = 0.75$. The fracture toughness at the onset of crack growth increases with increasing relative density (decreasing hole diameter) and for $\bar{\rho} = 0.75$, the fracture toughness at the onset of crack growth for the micro-architectured material is above that of the parent material. Thus, the crack blunting effects dominate for $\bar{\rho} = 0.75$ while hole-hole interaction effects dominate for the $\bar{\rho} = 0.25$ micro-architectured material.

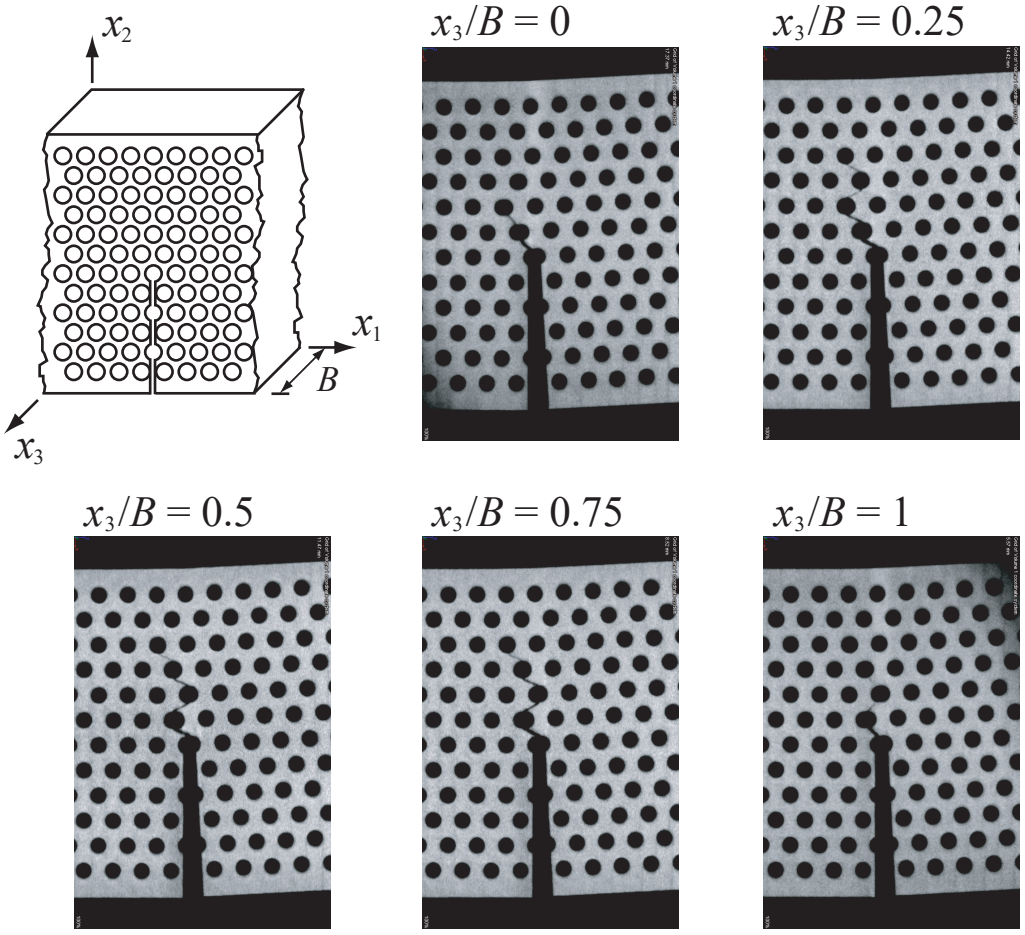


Figure 5: X-ray tomography images showing the thumbnail shape of a crack propagating in the single-edge notch bending specimen of a micro-architectured material with a relative density, $\bar{\rho} = 0.75$ and a cell size, $d + t = 2.2$mm. The crack appears shorter at the free surfaces ($x_3/B = 0$ and 1) and longer in the middle of the specimen ($x_3/B = 0.5$).

Surface images of deformed specimens of micro-architectured materials with relative densities $\bar{\rho} = 0.25$ and 0.75 are shown in Fig. 4. The crack path in both specimens is marked by a dashed red line. In both cases, crack growth initiates from the hole at the initial crack tip and the advancing crack tip oscillates from left to right but always stays close to the center line of the specimen. Importantly, the images show that the mode of

fracture in both the low and high relative density cases is similar with a crack propagating in the solid between the holes with negligible necking of the ligaments, i.e. the fracture mode of the micro-architectured material is not coalescence of the holes associated with necking of the ligaments but due to ductile fracture of the ligaments. To visualize the shape of the crack in the through-thickness direction, X-ray tomography images of deformed specimens were acquired. The X-ray tomography images for the specimen of a micro-architectured material with $\bar{\rho} = 0.75$ are shown in Fig. 5, where each image represents a slice of the specimen through the thickness. The images in Fig. 5 clearly show a thumbnail shaped crack; at the free surfaces ($x_3/B = 0$ and 1) only two cell walls appear broken, whereas the images taken from within the specimen ($x_3/B = 0.25$, 0.5 and 0.75) reveal that four cell walls are fractured. This suggests that despite the presence of the holes, there is sufficient build-up of hydrostatic stress within the $\bar{\rho} = 0.75$ micro-architectured material for a thumbnail crack front to develop much like in bulk materials.

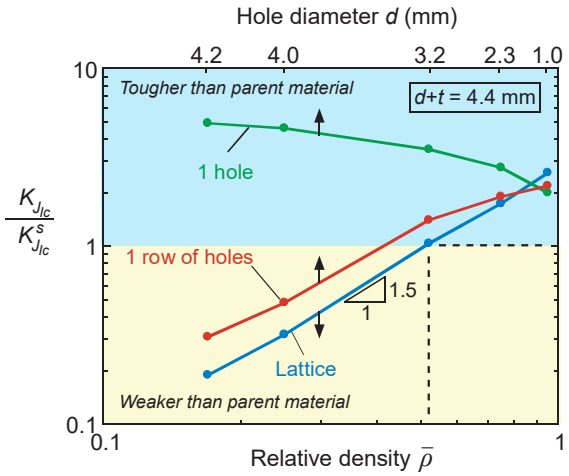


Figure 6: The normalized fracture toughness as a function of relative density, $\bar{\rho}$, for micro-architectured materials. Results for specimens with a single hole and for those with a row of holes are also plotted as a function of the hole diameter, $d$. The hole spacing, $d + t = 4.4$mm, for both the specimens with a row of holes and the micro-architectured materials.

The measured fracture toughness of all three types of specimens tested are compared in Fig. 6, where $K_{J_{IC}}/K^{S}_{J_{IC}}$ is plotted as a function of the relative density for micro-architectured materials and as a function of the hole diameter for single hole specimens and for those with a row of holes (note the double x-axis). The three types of specimen have a comparable fracture toughness when $d = 1$mm. Note that $d = 1$mm is small compared to the hole spacing, $d+t = 4.4$mm and consequently hole-hole interaction effects are negligible. For $d > 1$mm, hole-hole interaction effects are significant and specimens with a row of holes and micro-architectured materials have a fracture toughness inferior to that of single hole specimens. Furthermore, the fracture toughness of specimens with a row of holes is slightly greater than that of micro-architectured materials. This is due to the orientation of the

ligaments; specimens with a row of holes have their cell walls aligned with the direction of maximum tensile stress whereas micro-architectured material have ligaments oriented at 30° from the loading direction, see Fig. 2. The most striking result in Fig. 6 is that a micro-architectured material with $\bar{\rho} = 0.52$ has the same fracture toughness as that of the parent material, see dashed line in Fig. 6. In other words, the micro-architectured material is $\approx 50\%$ lighter than the parent material but possesses the same value of fracture toughness. This remarkable result was obtained here for a micro-architectured material with a hole spacing $d+t = 4.4$mm and next, we examine the influence of the parameter, $d+t$, upon the fracture toughness of micro-architectured materials.

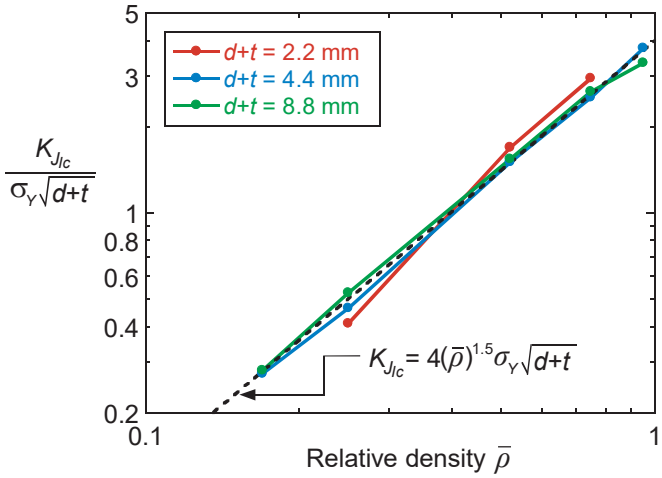


Figure 7: The normalized fracture toughness as a function of relative density, $\bar{\rho}$, for micro-architectured materials with three selected values of hole spacing, $d+t$, obtained using three-point bending fracture test of single-edge notch specimens.

Dimensional analysis suggests that the fracture toughness of micro-architectured materials scales with $\sqrt{l}$, see Eq. (1). To investigate this, additional micro-architectured materials were manufactured with the dimensions shown in Fig. 2(a) increased by a factor of two. Hence, these five micro-architectured materials had the same values of relative density as those presented in Fig. 6, but with a hole spacing $d+t = 8.8$mm instead of 4.4mm. Likewise, smaller micro-architectured materials were also prepared with the dimensions shown in Fig. 2(a) reduced by a factor of two. Due to manufacturing limitations, only three small micro-architectured materials with $d+t = 2.2$mm were manufactured: $\bar{\rho} = 0.25$, 0.52 and 0.75. The normalized fracture toughness of micro-architectured materials with $d+t = 2.2$, 4.4 and 8.8mm are plotted in Fig. 7 as a function of relative density. Note that here $K_{J_{IC}}$ is normalized by $\sigma_Y\sqrt{d+t}$, where $\sigma_Y$ is the yield strength of the parent material. Using this normalization, the results for the three different values of $d+t$ collapse onto a single line. This confirms that the fracture toughness scales with the square-root of the cell size. Moreover, a linear fit to the data in Fig. 7 suggests that

$$K_{J_{IC}} = 4\,(\bar{\rho})^{1.5}\,\sigma_Y\sqrt{d+t} \tag{5}$$

The value of the exponent, 1.5, is the same as that for aluminum metal foams (McCullough et al., 1999; Olurin et al., 2000); it is less than the value of 2 obtained for hexagonal micro-architectured materials (Gibson and Ashby, 1999; Fleck and Qiu, 2007) which are bending-dominated micro-architectured materials but greater than the value of 1 obtained for the stretch-dominated octet trusses (O'Masta et al., 2017). We however emphasize that, over the very large relative density range investigated here there is no a-priori reason to expect the usual bending/stretching dominated scaling that exists for low relative density micro-architectured and lattice materials. The physical reason behind the existence of such a power-law scaling in Fig. 7 needs further investigation.

## 4. Numerical method

The experimental results suggest that the micro-architectured material investigated here has a high fracture toughness (in some cases exceeding that of the solid material). However, from the experiments which have complied with the usual ASTM:E1820-11 (2011) standard developed for solid metals, it remains unclear whether a $J-$field is present within the specimens and thus whether the experiments result in a valid fracture toughness measurement. To interrogate this issue here we report finite element calculations of fracture of these micro-architectured materials. The numerical method chosen is motivated by the observation reported in the preceding section that fracture of the micro-architectured material occurs via the propagation of a ductile crack between the holes of the micro-architectured material, i.e. we chose a constitutive framework for progressively cavitating ductile solid that has been widely employed to model ductile fracture in metals and alloys including Aluminum alloys.

The finite element calculations are carried out using our in-house data parallel finite element code, which is based on the dynamic principle of virtual work using a finite deformation Lagrangian convected coordinate formulation (Srivastava et al., 2014; Liu et al., 2019, 2020). In order to compare predictions with experiments, finite element calculations are carried out for single-edge notch specimens with a single hole, a row of holes and a hexagonal array of holes (micro-architectured material) subjected to three-point bending, Fig. 8. The overall in-plane (along $x$ and $y$ axes) dimensions of the single-edge notch specimen analyzed are the same as in experiments. However, the thickness, $B$, (dimension along $z$ axis) of the specimen in the calculations is taken to be 1mm and overall plane strain conditions are imposed on $z = 0$ and $z = B$ surfaces of the specimen. The $y$-displacement of the specimen is constrained at locations, $y = 0$, $x = 14$mm and $y = 0$, $x = 214$mm in the reference configuration to prevent rigid body motion. The finite element calculations are based on the dynamic principle of virtual work for numerical convenience but the focus here is on the quasi-static response, hence to minimize the wave effects a time varying velocity, $V_y(t)$, in the negative $y$ direction is applied at location, $y = 50$mm, $x = 114$mm, that follows the relation:

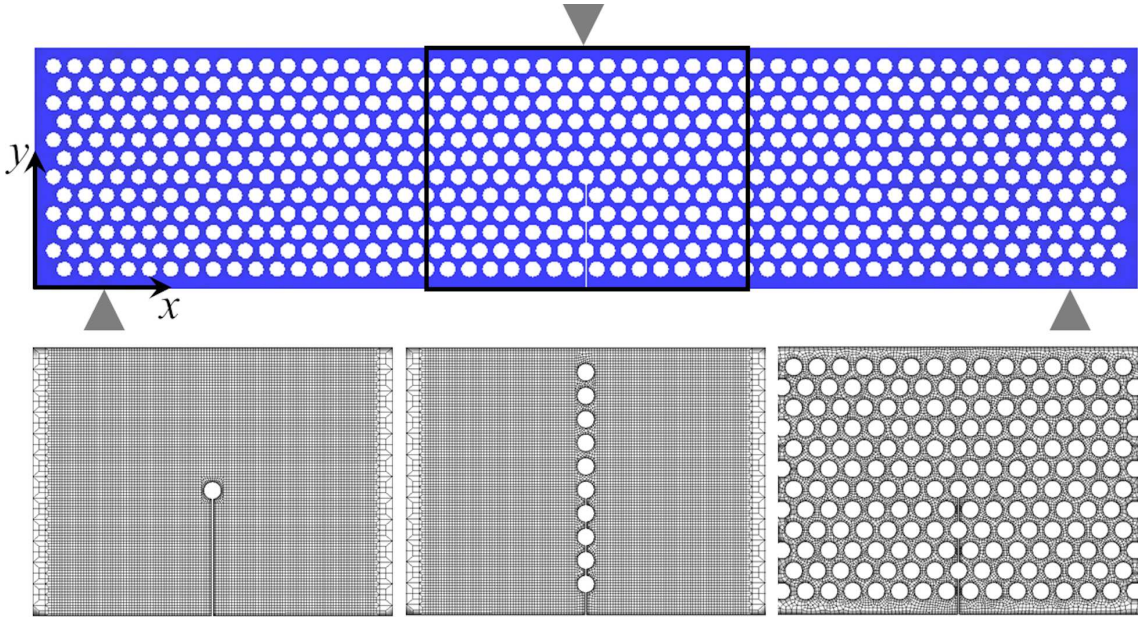


Figure 8: Sketch of the single-edge notch specimen of a micro-architectured material with a hexagonal array of holes subjected to three-point bending (top). Zoomed view of the finite element mesh in single-edge notch specimens with a single hole, a row of holes and a hexagonal array of holes (bottom left-right).

$$V_y(t) = \begin{cases} V_y^0 t/t_r & \text{if} \quad t \leq t_r \\ V_y^0 & \text{if} \quad t > t_r \end{cases} \tag{6}$$

where, $t$ is the analysis time, $t_r$ is the rise time and $V_y^0$ is the final velocity of the punch for $t > t_r$. In the calculations, $t_r = 1.0 \times 10^{-3}$s and $V_y^0 = 1.0 \times 10^3$mm/s (along negative $y$ axis) is used.

The constitutive framework for a progressively cavitating ductile solid is used in the form of a modified Gurson constitutive relation (Gurson, 1977; Tvergaard and Needleman, 1984; Chu and Needleman, 1980), with the flow potential having the form

$$\Phi = \frac{\sigma_e^2}{\bar{\sigma}^2} + 2q_1 f^* \cosh\left(\frac{3q_2\sigma_h}{2\bar{\sigma}}\right) - 1 - (q_1 f^*)^2 \tag{7}$$

with $q_1$, $q_2$ being parameters introduced in Tvergaard (1981, 1982b). In Eq. (7), $\bar{\sigma}$ is the matrix flow strength, $\sigma_e$ is the Mises effective stress, $\sigma_h$ is the hydrostatic stress and $f^*$ is the effective void volume fraction given by

$$f^* = \begin{cases} f, & f < f_c \\ f_c + (1/q_1 - f_c)(f - f_c)/(f_f - f_c), & f \geq f_c \end{cases} \tag{8}$$

where, $f$ is the void volume fraction, $f_c$ is the critical void volume fraction to void coalescence and $f_f$ is the void volume fraction at failure.

The rate of deformation tensor, $\mathbf{d}$, is given as the sum of an elastic part, $\mathbf{d}^e$ and a viscoplastic part, $\mathbf{d}^p$. The elastic part is $\mathbf{d}^e = \mathbf{L}^{-1} : \hat{\boldsymbol{\sigma}}$, where $\hat{\boldsymbol{\sigma}}$ is the Jaumann rate of Cauchy stress and $\mathbf{L}$ is the tensor of isotropic elastic moduli as characterized by the Young's modulus, $E$, and Poisson's ratio, $\nu$. The viscoplastic part, $\mathbf{d}^p$, is given as (Pan et al., 1983)

$$\mathbf{d}^p = \left[\frac{(1-f)\bar{\sigma}\dot{\bar{\varepsilon}}}{\boldsymbol{\sigma} : \frac{\partial \Phi}{\partial \boldsymbol{\sigma}}}\right] \frac{\partial \Phi}{\partial \boldsymbol{\sigma}} \tag{9}$$

with the matrix plastic strain rate, $\dot{\bar{\varepsilon}}$, having the form

$$\dot{\bar{\varepsilon}} = \dot{\varepsilon}_0 \left[\frac{\bar{\sigma}}{g(\bar{\varepsilon})}\right]^{1/m} \quad , \quad g(\bar{\varepsilon}) = \sigma_0 \left[1 + \bar{\varepsilon}/\varepsilon_0\right]^N \tag{10}$$

where $\bar{\varepsilon} = \int \dot{\bar{\varepsilon}} dt$, $\dot{\varepsilon}_0$ is the reference strain rate, $m$ is the strain rate sensitivity, $\sigma_0$ is the reference flow stress, $N$ is the strain hardening exponent and $\varepsilon_0 = \sigma_0/E$.

The evolution of the void volume fraction, $f$, is governed by

$$\dot{f} = (1-f)\mathbf{d}^p : \mathbf{I} + \dot{f}_{nucl} \tag{11}$$

where the first term on the right hand side of Eq. (11) accounts for void growth and the second term accounts for void nucleation. Void nucleation is assumed to be controlled by the accumulated plastic strain (Chu and Needleman, 1980),

$$\dot{f}_{nucl} = \frac{f_N}{s_N\sqrt{2\pi}} \exp\left[-\frac{1}{2}\left(\frac{\bar{\varepsilon} - \varepsilon_N}{s_N}\right)^2\right] \dot{\bar{\varepsilon}} \tag{12}$$

with $f_N$, $s_N$ and $\varepsilon_N$ being constitutive parameters.

The constitutive framework for a progressively cavitating ductile solid as used here, contains several constitutive parameters that need to be determined. We first focus on the constitutive parameters that characterize the elastic-viscoplastic response of a fully dense 6082-T6 aluminum alloy. To this end, we first fix upon the values, $E = 70$GPa and $\nu = 0.3$, and obtain the remaining parameters in Eq. (10) using the portion of the experimentally obtained uniaxial stress-strain curve before the onset of necking. The values of the constitutive parameters that best describe the overall stress-strain response of the as-received fully dense material are: $\sigma_0 = 280$MPa, $\varepsilon_0 = \sigma_0/E = 0.00429$, $N = 0.64$, $m = 0.002$ and $\dot{\varepsilon}_0 = 0.1\text{s}^{-1}$. Next, the values of $q_1 = 1.5$ and $q_2 = 1.0$ in Eq. (7) are taken from Faleskog et al. (1998), and the values of $f_c = 0.05$ and $f_f = 0.1$ in Eq. (8) are taken following Hosseini and Hadidi-Moud (2016). Finally, the values of the initial void volume fraction (value of $f$ at $t = 0$), $f_0 = 0.005$, and the values of $\varepsilon_N = 0.05$, $s_N = 0.01$ and $f_N = 0.02$ in Eq. (12) are obtained by minimizing the mean squared error between the predicted and experimentally obtained force versus CMOD response of two single-edge notch bending specimens of micro-architectured materials with relative densities, $\bar{\rho} = 0.25$ and $0.75$, using the Nelder-Mead simplex algorithm and following a procedure similar to that of Gerbig et al. (2017); Liu et al. (2020).

The finite element calculations use twenty-node brick elements and eight point Gaussian integration in each element for integrating the internal force contributions, and twenty-seven point Gaussian integration for the element mass matrix. Lumped masses are used so that the mass matrix is diagonal. The discretized equations are integrated using the explicit Newmark $\beta$-method with $\beta = 0$ (Belytschko et al., 1976). The constitutive updating is based on the rate tangent modulus method (Peirce et al., 1984), while material failure is implemented via the element vanishing technique (Tvergaard, 1982a). Representative finite element meshes for single-edge notch specimens with a single hole, a row of holes and a hexagonal array of holes are shown in Fig. 8. The finite element meshes are all generated using a single element in the through-thickness direction (along $z$ axis). A fine in-plane (along $x$ and $y$ axes) mesh is used with a fixed element size of 0.5mm in a $60 \times 50\text{mm}^2$ region near the center of the specimen.

## 5. Numerical results

The reaction force at the mid-span versus CMOD curves, of single-edge notch specimens with a single hole, a row of holes and a hexagonal array of holes (micro-architectured material) are shown in Fig. 9. Similar to the experimental results presented in Fig. 3, the predicted three-point bending response of all the specimens reported in Fig. 9 displays an elastic-plastic response up to peak load, $F_{pk}$, followed by a softening response due to crack growth initiation. The predicted three-point bending response of the specimens with a row of holes and micro-architectured materials up to $F_{pk}$ is in close quantitative agreement with the experimentally observed responses for all hole diameters and spacings. However, for the specimens with a single hole the predicted three-point bending response differs somewhat from that of observations for certain hole diameters. For example, for a specimen with a single hole of diameter, $d = 2.3$mm the measured $F_{pk} \approx 29$kN and CMOD at $F_{pk}$ is $\approx 1$mm while in the finite element calculations $F_{pk} \approx 37$kN and CMOD at $F_{pk}$ is $\approx 1.4$mm. On the other hand, for a specimen with a single hole of diameter, $d = 4.0$mm, both experimental and finite element results are in close agreement.

In the experiments, the $J-R$ curves were evaluated using the elastic compliance method as given in ASTM:E1820-11 (2011). However, the $J$-integral can also be directly obtained from the finite element results. Recall that, for a two dimensional, planar, nonlinear elastic material, under the assumption of small displacement gradient and with body forces neglected, the $J$-integral is given by (Rice, 1968)

$$J = -\int_C (\sigma_{ij}\frac{\partial u_i}{\partial x_1} - W\delta_{1j})n_j\, ds \tag{13}$$

in terms of the stress $\sigma_{ij}$, displacement $u_i$, the increment of arc length along the path $ds$, strain energy $W$ and the outward normal to the path $n_j$. In order to determine the value of the $J$-integral from the finite element results, it is convenient to re-write the contour integral as an equivalent area integral. The energy release rate, $J$-integral, can then be calculated using the relation (Li et al., 1985)

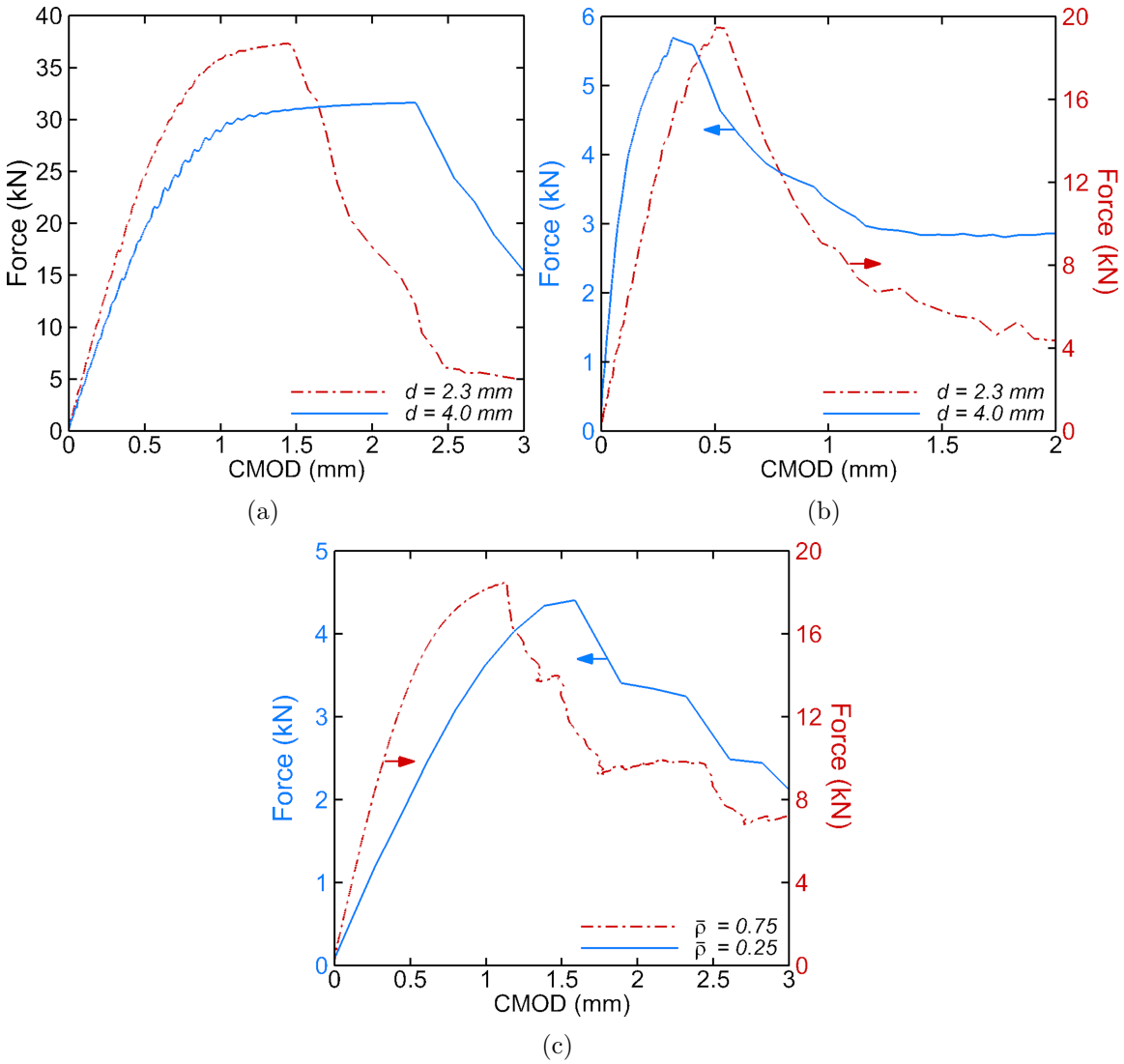


Figure 9: Predicted force versus crack mouth opening displacement (CMOD) response of single-edge notch specimens with (a) a single hole, (b) a row of holes and (c) a hexagonal array of holes (micro-architectured material) subjected to three-point bending. The hole diameter, $d = 2.3$mm, for micro-architectured material with relative density, $\bar{\rho} = 0.75$, and $d = 4.0$mm for $\bar{\rho} = 0.25$. The hole spacing, $d + t = 4.4$mm, for the specimens with a row of holes and the micro-architectured materials.

$$J = \int_A (\sigma_{ij} \frac{\partial u_i}{\partial x_1} - W\delta_{1j}) \frac{\partial Q_1}{\partial x_j} \, dA \tag{14}$$

where $Q_1$ is a smooth weighting function defined on the domain.

The dependence of the $J$-integral as obtained from the finite element results using Eq. (14) upon the radius of contours surrounding the initial notch tip of the single-edge notch bend specimens with a single hole, a row of holes and a hexagonal array of holes is

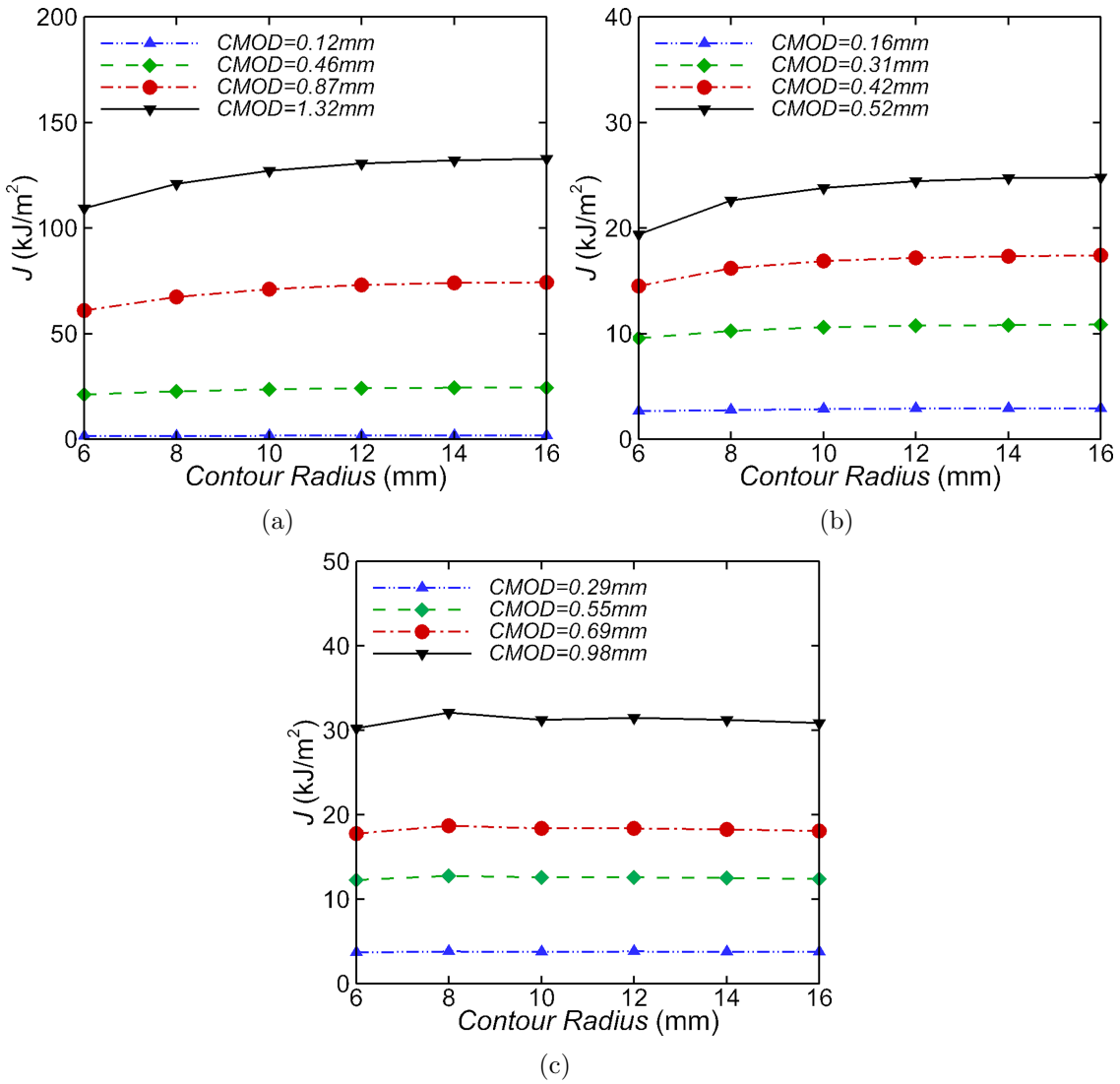


Figure 10: Predicted dependence of the value of $J$-integral on the radii of circular contour surrounding the initial notch tip of the single-edge notch specimens with (a) a single hole, (b) a row of holes and (c) a hexagonal array of holes (micro-architectured material) with relative density, $\bar{\rho} = 0.75$, subjected to three-point bending. The hole diameter, $d = 2.3$mm, for all the specimens and hole spacing, $d + t = 4.4$mm, for the specimens with a row of holes and the micro-architectured material.

shown in Fig. 10. As shown in Figs. 10(a) and (b), for the specimens with a single hole and a row of holes the value of $J$-integral is slightly path dependent. Also, the extent of path dependence of $J$-integral increases with increasing CMOD. However, for contour radius $\geq 12$mm the value of $J$-integral tends to saturate. The path dependence of $J$-integral, such that the value of $J$-integral initially increases with increasing contour radius, under finite deformation where proportional loading is not guaranteed is not entirely unexpected (Carka and Landis, 2011). However, for the micro-architectured material, Fig. 10(c), the

value of $J$-integral is almost path independent. Thus, a contour radius of 12mm is selected for evaluating $J$-integral for all the specimens. A more detailed discussion on the existence of a $J$ field and the resulting values of $J$-integral in micro-architectured materials is given in Section 6.

The value of $J_{IC}$, a measure of crack growth initiation toughness, is defined as the value of the contour integral $J$ corresponding to which crack growth initiation is predicted in the finite element calculations. The value of fracture toughness in terms of critical stress intensity factor, $K_{J_{IC}}$, is then obtained using the relation given in Eq. (4). Apart from the direct computation of $K_{J_{IC}}$ via the $J$-integral, the value of $K_{J_{IC}}$ is also obtained by direct application of the ASTM:E1820-11 (2011) standard to the finite element results; however, instead of using the elastic compliance method to obtain crack length, the crack length was known immediately from the finite element results.

A comparison of the normalized fracture toughness, $K_{J_{IC}}/K^s_{J_{IC}}$, (i) as measured from three-point bending experiments, (ii) as predicted by post-processing of the finite element results using the ASTM:E1820-11 (2011) standard and (iii) as predicted by direct computation of $J$-integral for all three types of single-edge notch specimens are shown in Fig. 11. For all three specimens, the results are normalized by, $K^s_{J_{IC}}$, the experimentally obtained fracture toughness of the as-received plate of aluminum alloy 6082-T6. Very good agreement between the predicted fracture toughness from the finite element calculations by both evaluation procedures and the experimental results is noted. The biggest discrepancy between the finite element predictions and the experimental results is observed for specimens with a single hole of small diameter. This is consistent with the differences between the predictions in Fig. 9(a) and experimental measurements in Fig. 3(a).

## 6. Discussion

The mechanical properties of micro-architectured materials depend upon their topology. The effect of topology of micro-architectured materials upon the stiffness and strength is well documented, but optimizing their fracture toughness is a challenging and intriguing task. Here, we have presented the results of fracture toughness tests on micro-architectured materials that comprise a hexagonal array of holes drilled in the plates of an aluminum alloy. The fracture toughness of the micro-architectured materials considered here is governed by two competing mechanisms: crack blunting and hole-hole interaction. The holes act as crack arrestors and blunt the crack-tip so that increasing the hole diameter will result in an increase in the fracture toughness whereas for fixed hole spacings, increasing the hole diameter will result in increased hole-hole interactions and decrease the fracture toughness.

The competing effect of crack blunting and hole-hole interaction on the evolution of damage in micro-architectured materials is elucidated in Fig. 12. In the figure, the predicted distribution of porosity, $f$, near the initial notch of single-edge notch specimens of micro-architectured materials with $\bar{\rho} = 0.25$ ($d = 4.0$mm) and $\bar{\rho} = 0.75$ ($d = 2.3$mm) are shown post three-point bending to three values of CMOD. The hole spacing in both micro-architectured materials is fixed at $d + t = 4.4$mm. Prior to crack growth initiation, the increased porosity is spread over a larger area in the micro-architectured material with

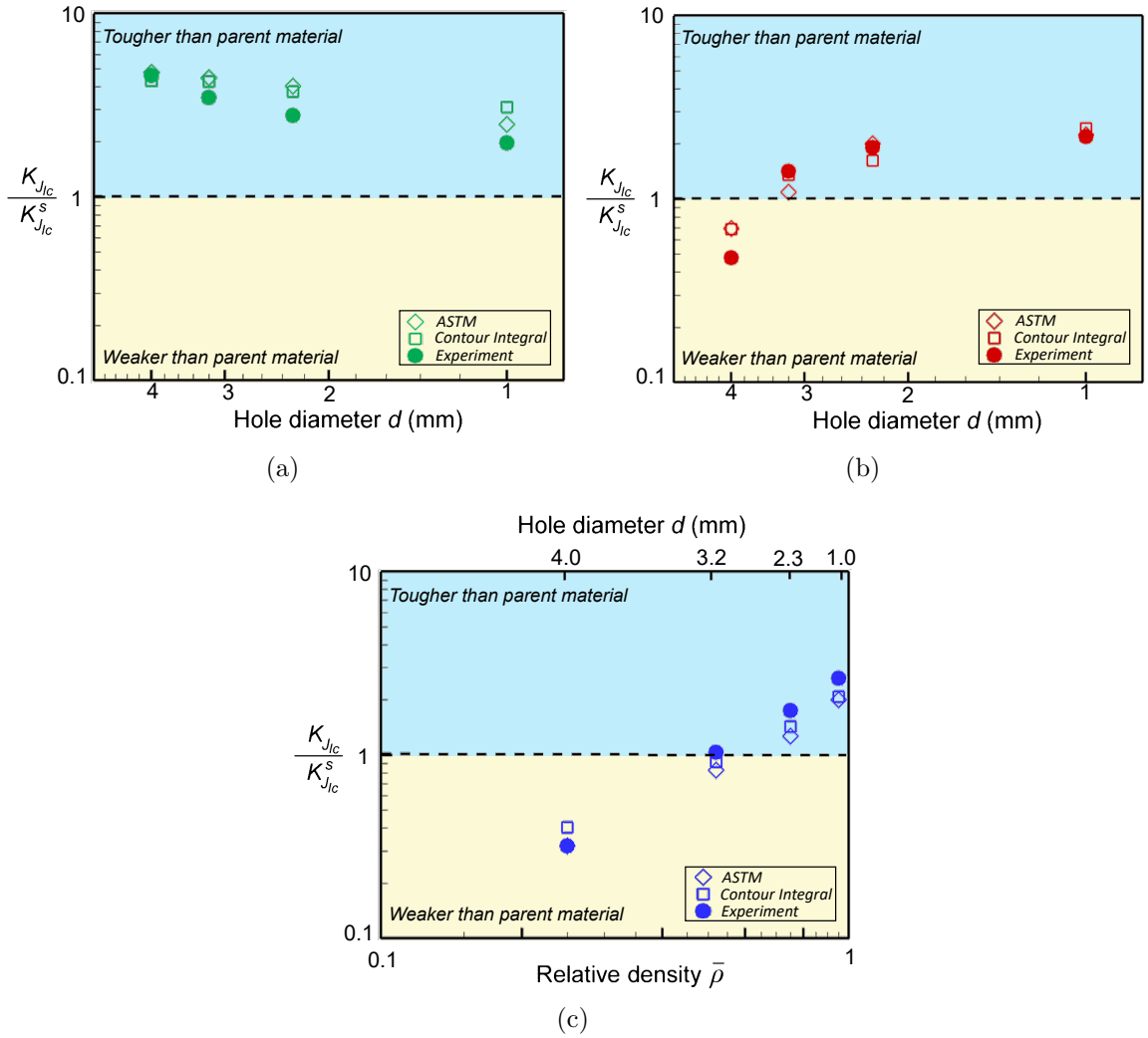


Figure 11: Comparison of the normalized fracture toughness measured from the three-point bending experiments (labeled 'Experiment') and computed from the post-processing of the finite element results using a procedure that mimics the ASTM:E1820-11 (2011) standard (labeled 'ASTM') and via direct computation of $J$-integral (labeled 'Contour Integral') for (a) specimens with a single hole of diameter, $d$, (b) specimens with a row of holes of diameter, $d$, and hole spacing, $d + t = 4.4$mm, and (c) micro-architectured materials with relative density, $\bar{\rho}$, and $d + t = 4.4$mm.

$\bar{\rho} = 0.25$ compared to the micro-architectured material with $\bar{\rho} = 0.75$ due to increased hole-hole interaction. Thus, the fracture toughness of the micro-architectured material with $\bar{\rho} = 0.25$ is less than that of the fracture toughness of the as-received plate of the parent material. On the other hand, due to an optimum balance of hole blunting and hole-hole interaction, the fracture toughness of the micro-architectured material with $\bar{\rho} = 0.75$ exceeds that of the fracture toughness of the parent material.

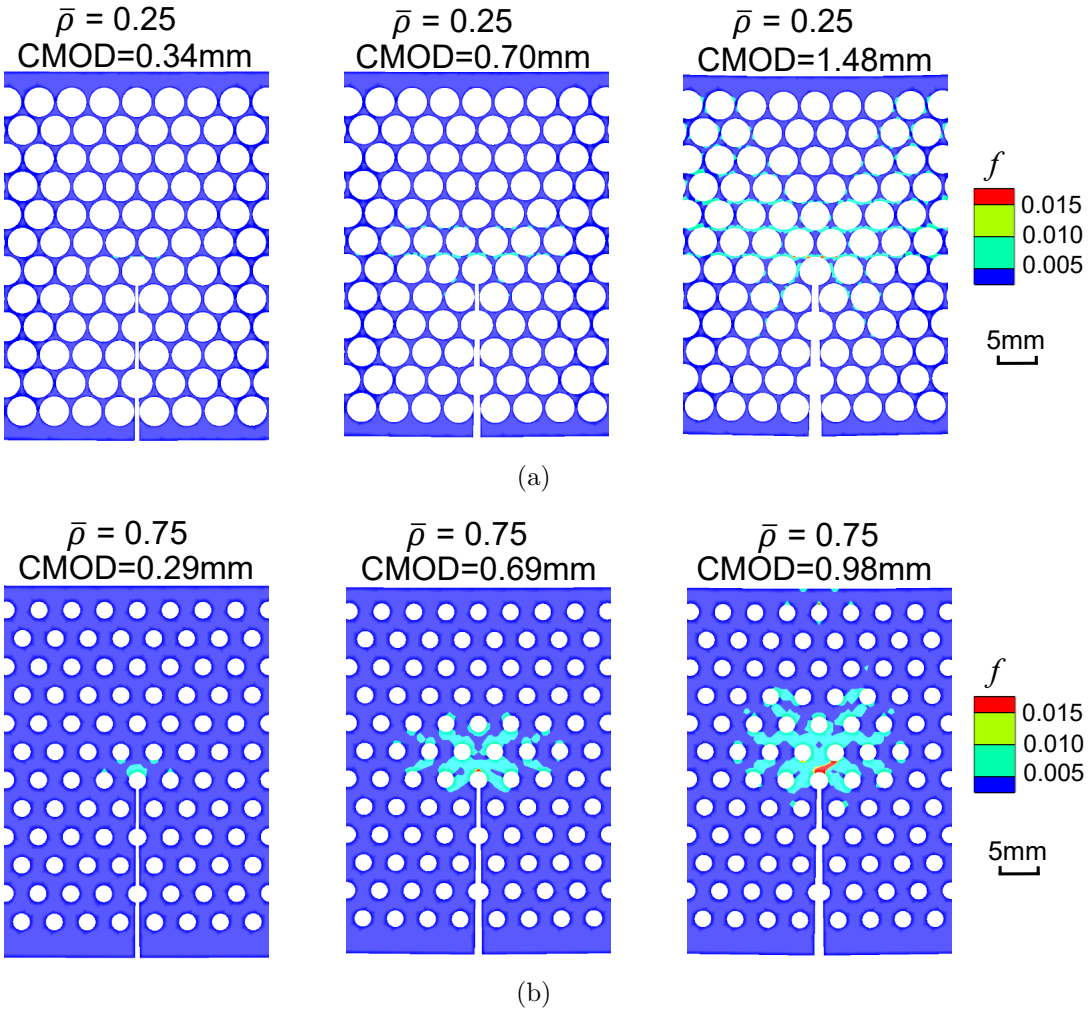


Figure 12: Predicted distribution of porosity, $f$, near the initial notch of single-edge notch specimens of micro-architectured materials with (a) relative density, $\bar{\rho} = 0.25$, post three-point bending to crack mouth opening displacement (CMOD) values 0.34, 0.70 and 1.48mm, and (b) $\bar{\rho} = 0.75$ post three-point bending to CMOD values 0.29, 0.69 and 0.98mm. The hole diameter, $d = 2.3$mm, for micro-architectured material with $\bar{\rho} = 0.75$ and $d = 4.0$mm for $\bar{\rho} = 0.25$. The hole spacing, $d + t = 4.4$mm, for both the micro-architectured materials.

The measured properties of the micro-architectured materials comprising a hexagonal array of holes are included in the material property charts, Fig. 1. The density of the micro-architectured materials is $\rho = \bar{\rho}\rho_s$, where the density of the parent material, $\rho_s = 2700\text{kg/m}^3$. In Fig. 1(b), the compressive strength of the micro-architectured material is the out-of-plane yield strength of magnitude $\bar{\rho}\sigma_Y$, where the yield strength of the parent material is $\sigma_Y = 280$MPa. It is clear from Fig. 1(a) that the micro-architectured materials of cell size $d + t = 8.8$mm are positioned at the outer boundary of the currently available material space. They outperform the toughest metals and they compete well with the toughest

natural materials. Recall that the measured fracture toughness of these micro-architectured materials scales with the square-root of the cell size $(d+t)$, Eq. (5). Consequently a hole spacing of $d+t = 30$mm, would lead to a micro-architectured material that is tougher than any known metals or natural materials as shown in Fig. 1. In conclusion, micro-architectured materials offer a combination of high strength and high fracture toughness that outperforms other lightweight materials of density less than 1000kg/m$^3$.

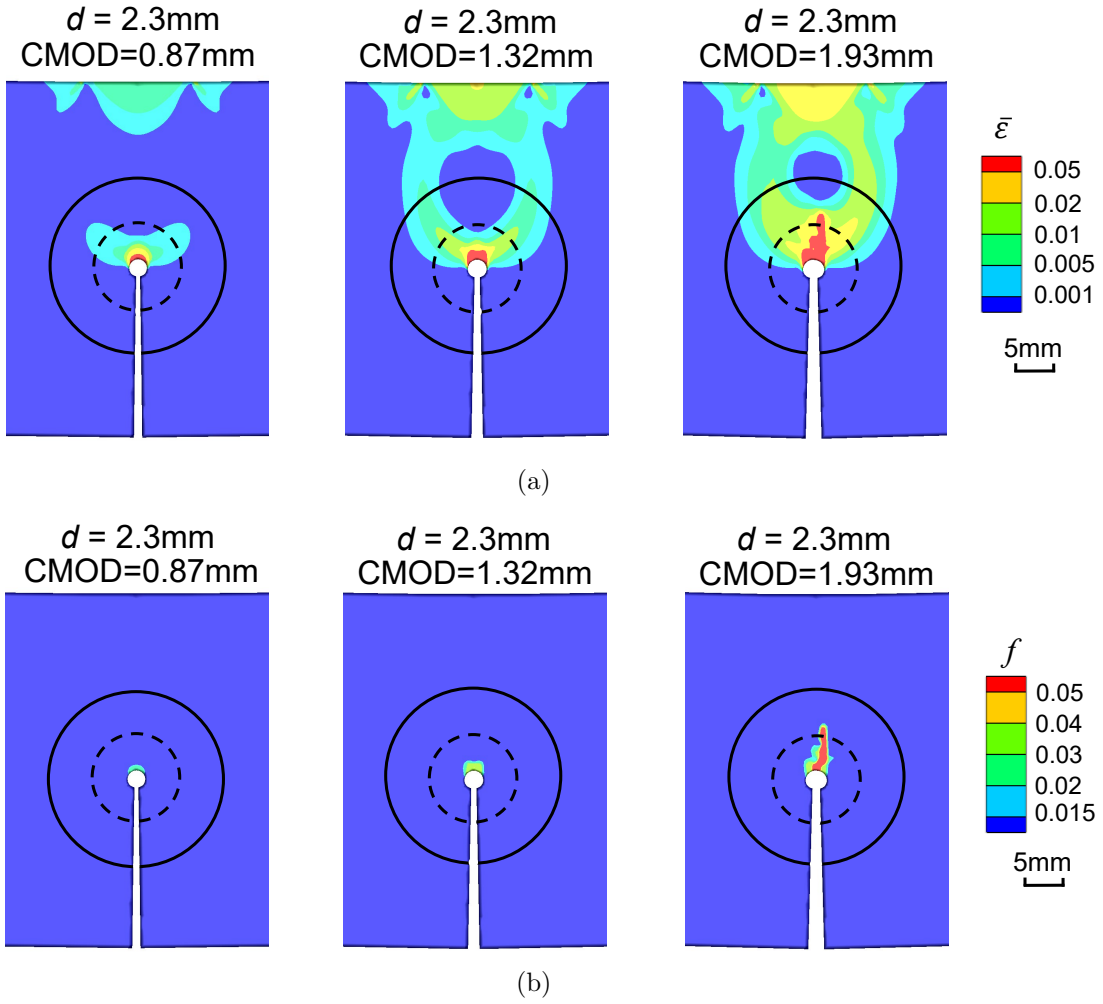


Figure 13: Predicted distribution of (a) equivalent plastic strain, $\bar{\varepsilon}$, and (b) porosity, $f$, near the initial notch in a single-edge notch specimen with a single hole of diameter, $d = 2.3$mm, post three-point bending to crack mouth opening displacement (CMOD) values 0.87, 1.32 and 1.93mm. A contour of radius, $r = 12$mm, is marked as solid black circle while a contour of radius, $r = 6$mm, is marked as dashed black circle.

In the present study, all the fracture tests of single-edge notch specimens under three-point bending were carried out in compliance with the ASTM:E1820-11 (2011) standard. The question arises: to what extent can a standard test procedure that was established for solid materials, be applicable to micro-architectured materials? Consider, for example,

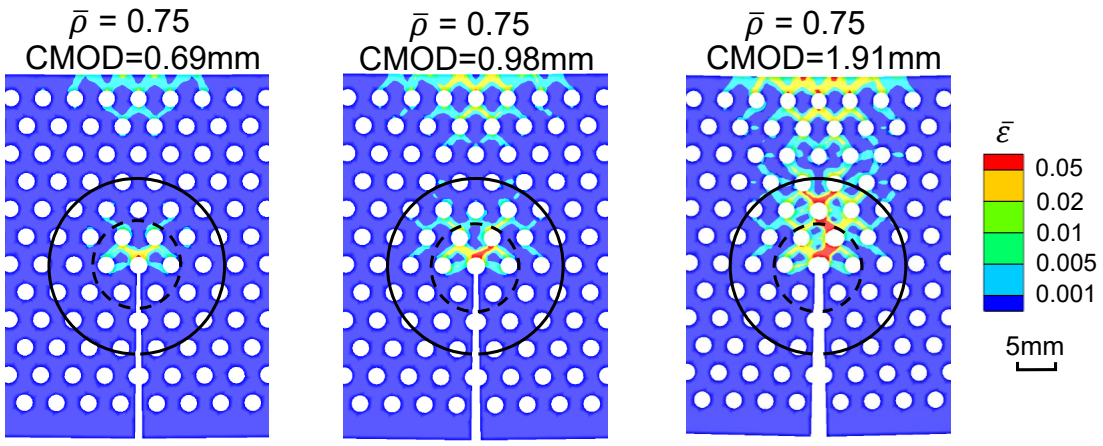


(a)

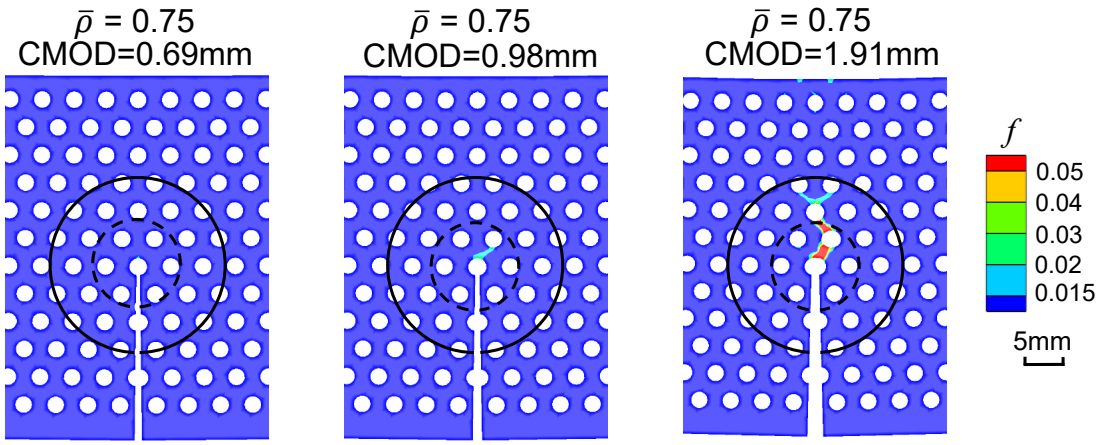


(b)

Figure 14: Predicted distribution of (a) equivalent plastic strain, $\bar{\varepsilon}$, and (b) porosity, $f$, near the initial notch in a single-edge notch specimen of micro-architectured material with relative density, $\bar{\rho} = 0.75$, post three-point bending to crack mouth opening displacement (CMOD) values 0.69, 0.98 and 1.91mm. The hole diameter, $d = 2.3$mm, in the micro-architectured material. A contour of radius, $r = 12$mm, is marked as solid black circle while a contour of radius, $r = 6$mm, is marked as dashed black circle. The contour plot in (b) is for the same case shown in Fig. 12(b) but plotted at greater values of CMOD.

the recent study by Tankasala et al. (2020) on an open cell aluminum alloy foam. They found that a zone of randomly failed struts develops ahead of the primary crack tip, and the size of this zone is similar to the plastic zone size. In such cases a crack tip $J$-field is absent at the initiation of crack growth and the measured $J_{IC}$ value cannot be treated as a material property even though the specimen size meets the usual criteria for $J$ validity. The ability of the value of $J$-integral to characterize the fracture properties is contingent upon the existence of a $J$-field near the crack tip which depends on whether the plastic zone fully encompasses the fracture process zone or not.

The predicted distribution of equivalent plastic strain, $\bar{\varepsilon}$, and of porosity, $f$, near the initial notch in a single-edge notch specimen with a single hole of diameter, $d = 2.3$mm, and in a single-edge notch specimen of a micro-architectured material with relative density, $\bar{\rho} = 0.75$ ($d = 2.3$mm), are shown in Figs. 13 and 14, respectively, for three-point bending to three values of CMOD. In Figs. 13 and 14, the first two values of CMOD are for $J < J_{IC}$ while the greatest value of CMOD corresponds to $J > J_{IC}$. For both the specimens with a single hole and the micro-architectured material, the fracture process zone size (i.e. $f \approx f_c$, where $f_c = 0.05$) is much smaller than the plastic zone size. Furthermore, the plastic zone size in the micro-architectured material is relatively small compared to that in the specimen with a single hole for comparable values of CMOD. The smaller plastic zone size in the micro-architectured material compared to the specimen with a single hole also rationalizes the observation in Fig. 10 that the value of $J$-integral in the micro-architectured material is less path dependent than the specimen with a single hole. The fact that the fracture process zone size is much smaller than the plastic zone size and the $J$-integral is almost path-independent in the single-edge notch specimens of micro-architectured material suggests that the measured fracture toughness, $J_{IC}$ or $K_{J_{IC}}$, can be treated as a material property. Furthermore, in the finite element calculations, the fracture toughness of single-edge notch specimens subjected to three-point bending is in agreement for the two procedures, one that mimics the ASTM:E1820-11 (2011) standard and via direct computation of $J$-integral.

Finally, to further establish that the fracture toughness of the micro-architectured materials obtained using single-edge notch bending specimens does indeed represent a useful material property which is independent of specimen geometry, we also carried out finite element calculations of ductile fracture in single-edge notch specimens of micro-architectured material under remote uniaxial tension. To this end, the single-edge notch specimens of micro-architectured material with the same geometry as in Fig. 8 are subjected to tensile loading along the $x$-axis. The fracture toughness is evaluated using the ASTM:E1820-11 (2011) standard and also via direct computation of $J$-integral. In the evaluation of fracture toughness of single-edge notch specimens subjected to tension following ASTM standard, a modified geometric function for single-edge notch tension specimen (Zhu, 2015) is utilized. A comparison of the normalized fracture toughness, $K_{J_{IC}}/K^S_{J_{IC}}$, predicted from finite element calculations of single-edge notch specimens subjected to tension and three-point bending are shown in Fig. 15(a). As shown in the figure, the fracture toughness of single-edge notch specimens of micro-architectured materials subjected to tension show the same scaling between fracture toughness and relative density as in three-point bending. The fracture toughness values obtained for single-edge notch tension specimens are slightly greater than that for single-edge notch bending specimens. This is because the crack-tip constraint in single-edge notch tension specimen is less than the single-edge notch bending specimen. However, we emphasize that the effect of this constraint on fracture toughness is relatively small suggesting that $K_{J_{IC}}$ is sufficient to characterize fracture in these micro-architectured materials. Also, similar to single-edge notch bending specimens, here as well, it is the competing effect of crack blunting and hole-hole interaction on the evolution of damage in micro-architectured materials, as elucidated in Fig. 15(b), that leads to the same scaling between fracture toughness and relative density.

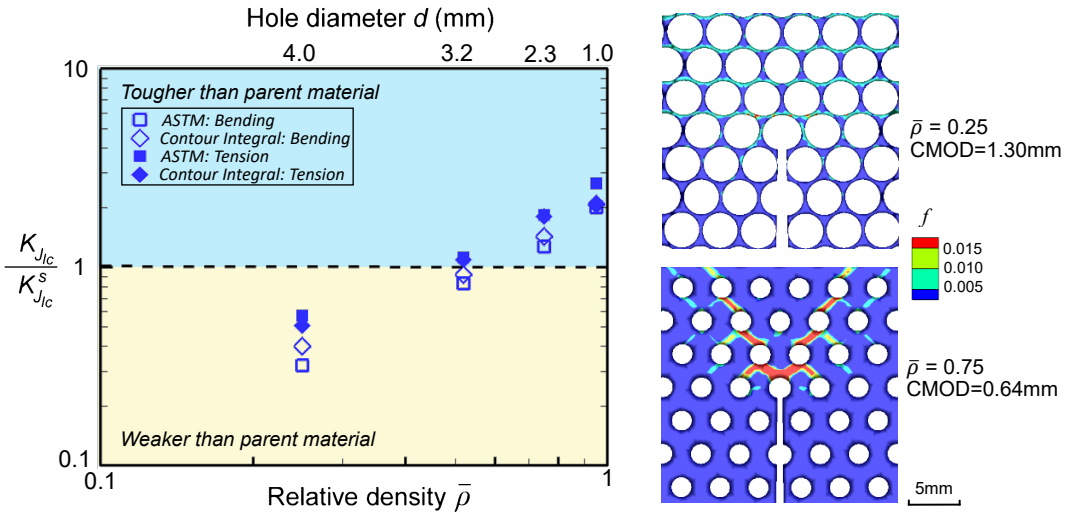


(a) (b)

Figure 15: (a) Comparison of the normalized fracture toughness predicted from finite element calculations of single-edge notch specimens of micro-architectured materials with relative density, $\bar{\rho}$, subjected to three-point bending and tension. The values of fracture toughness from finite element calculations are computed using a procedure that mimics the ASTM standard (labeled 'ASTM') and via direct computation of $J$-integral (labeled 'Contour Integral'). (b) Predicted distribution of porosity, $f$, near the initial notch of single-edge notch specimens of micro-architectured materials with relative density, $\bar{\rho} = 0.25$, post tensile loading to crack mouth opening displacement (CMOD) value 1.30mm and $\bar{\rho} = 0.75$ post tensile loading to CMOD= 0.64mm. The hole spacing, $d + t = 4.4$mm, for all micro-architectured materials.

## 7. Concluding remarks

We have investigated the fracture toughness of ductile micro-architectured materials to demonstrate their potential as a lightweight and tough material. The micro-architectured materials consisted of a hexagonal array of holes in a ductile material. The key conclusions are as follows:

- The fracture toughness of the micro-architectured materials with hexagonal array of holes in a ductile material increases with increasing relative density and with increasing cell size.
- A micro-architectured material with cell size, $d + t = 4.4$mm, and approximately 50% lighter than the parent material has the same fracture toughness as the parent material.
- The finite element calculations of three-point bending of single-edge notch specimens of micro-architectured materials show that in the micro-architectured materials the plastic zone fully encompasses the fracture process zone and a path independent value of $J$- integral can be obtained.

- The fracture toughness of the micro-architectured materials obtained from the finite element calculations of single-edge notch specimens subjected to three-point bending using a procedure similar to the experiments and via direct computation of $J$-integral are shown to be consistent with the experimental results.

- The fracture toughness of the micro-architectured materials obtained from the finite element calculations of single-edge notch specimens subjected to tension show the same scaling between fracture toughness and relative density as in three-point bending. This result confirms the validity of the measured fracture toughness as a useful material property.

- A comparison with other engineering materials show that the micro-architectured materials investigated expand the current material property space: it possesses an excellent combination of high strength and fracture toughness compared to other existing lightweight materials.

## Acknowledgments

VSD and NAF gratefully acknowledge financial support from the European Research Council (ERC) in the form of advanced grant, MULTILAT, GA669764 and the DARPA MCMA program (Grant Number W91CRB-10-1-005). AS gratefully acknowledges the financial support provided by the U.S. National Science Foundation grant CMMI - 1663130. LS gratefully acknowledges the financial support from the Academy of Finland (decision 322007). The authors are also thankful to S. Marshall and K. Bullman for manufacturing the specimens and to A. Heaver for his technical assistance. The large-scale finite element calculations reported on were carried out using high performance research computing resources provided by Texas A&M University.

## References

Anderson, T. L., 2017. Fracture mechanics: fundamentals and applications. CRC press.

Ashby, M. F., 2005. Materials selection in mechanical design. MRS Bull 30 (12), 995.

Ashby, M. F., 2011. Hybrid materials to expand the boundaries of material-property space. Journal of the American Ceramic Society 94, s3–s14.

ASTM:E1820-11, 2011. Standard test method for measurement of fracture toughness. ASTM International.

Begley, J., Logsdon, W., Landes, J., 1977. Ductile rupture blunt-notch fracture criterion. In: Flaw Growth and Fracture. ASTM International.

Belytschko, T., Chiapetta, R., Bartel, H., 1976. Efficient large scale non-linear transient analysis by finite elements. International Journal for Numerical Methods in Engineering 10 (3), 579–596.

Carka, D., Landis, C. M., 2011. On the path-dependence of the j-integral near a stationary crack in an elastic-plastic material. Journal of Applied Mechanics 78 (1), 011006.

Chu, C., Needleman, A., 1980. Void nucleation effects in biaxially stretched sheets. Journal of Engineering Materials and Technology(Transactions of the ASME) 102 (3), 249–256.

Dong, L., Deshpande, V., Wadley, H., 2015. Mechanical response of ti–6al–4v octet-truss lattice structures. International Journal of Solids and Structures 60, 107–124.

Faleskog, J., Gao, X., Shih, C. F., 1998. Cell model for nonlinear fracture analysis–i. micromechanics calibration. International Journal of Fracture 89 (4), 355–373.

Fleck, N. A., Deshpande, V. S., Ashby, M. F., 2010. Micro-architectured materials: past, present and future. Proceedings of the Royal Society A: Mathematical, Physical and Engineering Sciences 466 (2121), 2495–2516.

Fleck, N. A., Qiu, X., 2007. The damage tolerance of elastic–brittle, two-dimensional isotropic lattices. Journal of the Mechanics and Physics of Solids 55 (3), 562–588.

Gerbig, D., Srivastava, A., Osovski, S., Hector, L. G., Bower, A., 2017. Analysis and design of dual-phase steel microstructure for enhanced ductile fracture resistance. International Journal of Fracture, 1–24.

Gibson, L. J., Ashby, M. F., 1999. Cellular solids: structure and properties. Cambridge university press.

Gu, X. W., Greer, J. R., 2015. Ultra-strong architected cu meso-lattices. Extreme Mechanics Letters 2, 7–14.

Gurson, A. L., 1977. Plastic flow and fracture behavior of ductile materials incorporating void nucleation, growth, and interaction.

Hosseini, S., Hadidi-Moud, S., 2016. Application of the gtn model in ductile fracture prediction of 7075-t651 aluminum alloy. Journal of Solid Mechanics 8 (2), 326–333.

Huang, J., Gibson, L., 1991a. Fracture toughness of brittle foams. Acta metallurgica et materialia 39 (7), 1627–1636.

Huang, J., Gibson, L., 1991b. Fracture toughness of brittle honeycombs. Acta metallurgica et materialia 39 (7), 1617–1626.

Khaderi, S., Deshpande, V., Fleck, N., 2014. The stiffness and strength of the gyroid lattice. International Journal of Solids and Structures 51 (23-24), 3866–3877.

Khaderi, S. N., Scherer, M., Hall, C., Steiner, U., Ramamurty, U., Fleck, N. A., Deshpande, V. S., 2017. The indentation response of nickel nano double gyroid lattices. Extreme Mechanics Letters 10, 15–23.

Li, F. Z., Shih, C. F., Needleman, A., 1985. A comparison of methods for calculating energy release rates. Engineering Fracture Mechanics 21 (2), 405–421.

Liu, Y., Fan, D., Bhat, S. P., Srivastava, A., 2020. Ductile fracture of dual-phase steel sheets under bending. International Journal of Plasticity 125, 80–96.

Liu, Y., Zheng, X., Osovski, S., Srivastava, A., 2019. On the micromechanism of inclusion driven ductile fracture and its implications on fracture toughness. Journal of the Mechanics and Physics of Solids 130, 21–34.

Maiti, S., Ashby, M., Gibson, L., 1984. Fracture toughness of brittle cellular solids. Scripta Metallurgica 18 (3), 213–217.

McCullough, K. Y., Fleck, N. A., Ashby, M. F., 1999. Toughness of aluminium alloy foams. Acta materialia 47 (8), 2331–2343.

Olurin, O., Fleck, N. A., Ashby, M. F., 2000. Deformation and fracture of aluminium foams. Materials Science and Engineering: A 291 (1-2), 136–146.

O'Masta, M., Dong, L., St-Pierre, L., Wadley, H., Deshpande, V., 2017. The fracture toughness of octet-truss lattices. Journal of the Mechanics and Physics of Solids 98, 271–289.

Pan, J., Saje, M., Needleman, A., 1983. Localization of deformation in rate sensitive porous plastic solids. International Journal of Fracture 21 (4), 261–278.

Peirce, D., Shih, C. F., Needleman, A., 1984. A tangent modulus method for rate dependent solids. Computers & Structures 18 (5), 875–887.

Quintana-Alonso, I., Mai, S., Fleck, N., Oakes, D., Twigg, M., 2010. The fracture toughness of a cordierite square lattice. Acta Materialia 58 (1), 201–207.

Rice, J. R., 1968. A path independent integral and the approximate analysis of strain concentration by notches and cracks. Journal of applied mechanics 35 (2), 379–386.

Romijn, N. E., Fleck, N. A., 2007. The fracture toughness of planar lattices: imperfection sensitivity. Journal of the Mechanics and Physics of Solids 55 (12), 2538–2564.

Schmidt, I., Fleck, N., Oct 2001. Ductile fracture of two-dimensional cellular structures – dedicated to prof. dr.-ing. d. gross on the occasion of his 60th birthday. International Journal of Fracture 111 (4), 327–342.

Srivastava, A., Ponson, L., Osovski, S., Bouchaud, E., Tvergaard, V., Needleman, A., 2014. Effect of inclusion density on ductile fracture toughness and roughness. Journal of the Mechanics and Physics of Solids 63, 62–79.

Tankasala, H. C., Li, T., Seiler, P. E., Deshpande, V. S., A, F. N., 2020. An assessment of the j-integral test for a metallic foam. Journal of the Mechanics and Physics of Solids, Submitted for publication.

Tvergaard, V., 1981. Influence of voids on shear band instabilities under plane strain conditions. International Journal of fracture 17 (4), 389–407.

Tvergaard, V., 1982a. Influence of void nucleation on ductile shear fracture at a free surface. Journal of the Mechanics and Physics of Solids 30 (6), 399–425.

Tvergaard, V., 1982b. On localization in ductile materials containing spherical voids. International Journal of fracture 18 (4), 237–252.

Tvergaard, V., Needleman, A., 1984. Analysis of the cup-cone fracture in a round tensile bar. Acta metallurgica 32 (1), 157–169.

Yoda, M., 1987. The effect of the notch root radius on the j-integral fracture toughness under modes i, ii and iii loadings. Engineering fracture mechanics 26 (3), 425–431.

Zhu, X.-K., 2015. Advances in fracture toughness test methods for ductile materials in low-constraint conditions. Procedia Engineering 130, 784–802.